

Journal of Materials Chemistry A

Accepted Manuscript

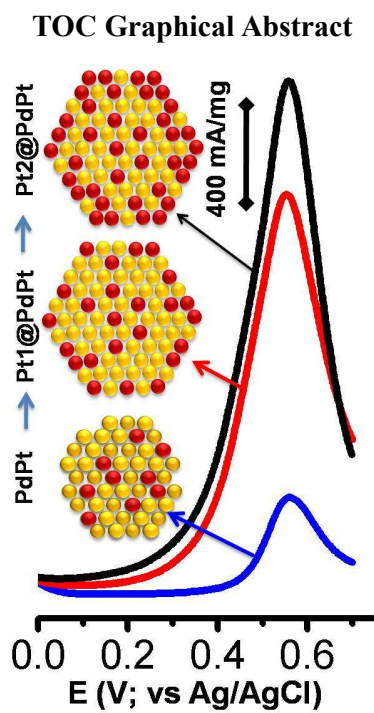


This is an *Accepted Manuscript*, which has been through the Royal Society of Chemistry peer review process and has been accepted for publication.

Accepted Manuscripts are published online shortly after acceptance, before technical editing, formatting and proof reading. Using this free service, authors can make their results available to the community, in citable form, before we publish the edited article. We will replace this *Accepted Manuscript* with the edited and formatted *Advance Article* as soon as it is available.

You can find more information about *Accepted Manuscripts* in the [Information for Authors](#).

Please note that technical editing may introduce minor changes to the text and/or graphics, which may alter content. The journal's standard [Terms & Conditions](#) and the [Ethical guidelines](#) still apply. In no event shall the Royal Society of Chemistry be held responsible for any errors or omissions in this *Accepted Manuscript* or any consequences arising from the use of any information it contains.



Pt skin structures over PdPt bimetallic nanocrystals show unusual enhancement in the methanol electrooxidation with mass activity of 2000 mA/mg_{Pt} and better stability.

Enhanced Methanol Electrooxidation at Pt skin@PdPt Nanocrystals

Bhalchandra Kakade^a, Indrajit Patil^a, Loganathan Moorthi^a, and Anita Swami^b*

^aSRM Research Institute, SRM University, Kattankulathur, Tamil Nadu, India 603 203.

Fax: (+91) 44-2745 6702; Tel: (+91) 44-2741 7920.

^bDepartment of Chemistry, SRM University, Kattankulathur, Tamil Nadu 603 203.

E-mail: bhalchandrakakade@gmail.com

KEYWORDS: Pt skin structure, Alloy, methanol electrooxidation, stability, synergistic effects

BRIEFS: An Unprecedented Methanol Electrooxidation by Pt skin@PdPt Nanocrystals

Abstract

Pt skin growth over PdPt alloy nanocrystals has been described using simple wet chemical method, where a layer-by-layer epitaxial deposition of Pt on PdPt could be understood by Stransky-Krastanov mechanism. Initial PdPt alloy nanocrystals grown in a simple wet-chemical method, in presence of a reducing solvent like N-methyl pyrrolidone (NMP) and stabilizer like polyvinyl pyrrolidone (PVP), have been used as substrate for secondary growth of Pt thin layer. Surface changes have been observed during step-by-step growth of polyhedral Pt skin@PdPt nanocrystals originating from nearly octahedral geometries of PdPt. The methanol electrooxidation activities of two different Pt skin@PdPt nanostructures have been compared with PdPt nanocrystals with similar composition but without skin structures and commercial RuPt catalysts. A gain factor of 8 towards electrooxidation of methanol in acidic media with activities of 1950 mA/mg_{Pt} and 3.1 mA/cm²_{Pt} (with lower onset potential compared to RuPt commercial catalyst), which is believed to be much higher compared to that of previous reports and state-of-art RuPt/C catalysts, indicating better surface properties and core-alloy formation along with improved intraparticle active interfacial sites. Additionally,

exciting results of electrooxidation of ethanol and ethylene glycol with 70% and 58% activity retentions respectively are also found, demonstrating a facile C-C breaking in such C2 type alcohols.

Introduction

Noble metal nanocrystals like Pd and Pt have shown unique importance in both the perspectives as fundamental research and energy technology development due to their unique catalytic properties like hydrogen separation, methanol oxidation (MOR) and oxygen reduction (ORR) [1-12]. Also, in the search of alternative means to generate energy, direct-methanol fuel cell (DMFC) is one of the most promising candidates due to their theoretical higher energy densities and Pt or Pt-based catalysts, especially RuPt are known to display the best catalytic behavior for methanol electro-oxidation [13]. Hence, there has been increasing demand for enhancing their catalytic activities during few decades by systematic tailoring their shapes and sizes using various approaches [3-10,14-19]. However, the combination of two metals into alloy is an important approach for tailoring the electronic and geometric heterostructures to enhance the activity and sensitivity [20-27]. Further, bimetallic alloys of Pt (with metals like Cu, Co, Ni, Pd, Fe, Ru etc) improve not only oxygen reduction reaction (ORR) activity at the cathode but also act as best anodic surface for carbon monoxide (CO) tolerance [28-34]. Alternatively, reducing the consumption of precious Pt metal or searching for new low cost catalyst (Pt-free) are two possible approaches to accelerate the practical application of DMFC.

Hence, a simple and affordable methodology to obtain such noble metals and their alloy nanocrystals with required catalytic activities is essential to surmount the current impediments in the fuel cell technologies. Plenty of combinations, especially, of

Pd and Pt have been obtained using various recipes of reducing and stabilizing agents so far [1-11,18]. For example, heterostructures of PdPt can generally be prepared by either successive co-reduction of both the ionic species [28-40], or a seed-mediated growth method [41,42] and variety of heterostructures ranging from hollow nanocubes, nanocages, core-shell or an epitaxial growth of Pt over Pd can be obtained to tune their catalytic activity towards methanol oxidation. Interestingly, Pt-on-Pd bimetallic nanodendrites with highly branched shapes represent a novel hybrid type of structure and have shown exciting electrocatalysis with high activity for ORR and MeOH oxidation [20,24,43]. In yet another report of CuCoPt ternary particles, Cu was galvanically removed from the CuCoPt particles after potential cycles to form the nanostructures having Pt and Co enriched surfaces and compressed surface strain, which enhances the catalytic activity [44]. Similarly, Sasaki *et. al.* [45] and Manthiram *et. al.*, [46] have also shown a galvanic replacement of Cu by Pt to make noble metal-rich nanocrystals to improve the catalytic activities with concomitant protection to non-noble core-metal under harsh conditions. However, the effect of electronic structure variation on methanol oxidation or oxygen reduction due to noble-non noble metal interactions in case of core-shell particles is negligible since the actual catalytic surface is far away from the alloy interface. This would hamper not only the catalytic activity but also contribute to the loss due to the effect of unexposed core-metal. Also, unlike a traditional Pd@Pt core-shell or more special Pt-on-Pd nanodendrites, a more homogeneous alloy or Pt skin@alloy system will drastically enhance the catalytic activity owing to the better intermetallic bonding and easy communication with reacting molecules and reactions at surface, which in turn might lead to a charge separation during MeOH electrooxidation [38,47]. Therefore, alloy or noble metal skin@alloy [48]

systems or nanoframe network [32,44,49,50] could be an interesting system to emphasize an appropriate correlation between the catalytic activity and electronic structure.

In the present report, we describe two-step facile method for the synthesis of Pt skin@PdPt using layer-by-layer epitaxial deposition of Pt on Pd rich PdPt alloy nanocrystals. Initial PdPt alloy polyhedrons grown in a simple co-reduction process, in presence of a reducing solvent like N-methyl pyrrolidone (NMP) and capping agent like polyvinyl pyrrolidone (PVP), have been used as substrate seed for secondary growth of Pt thin layer. Besides, electrooxidation of these Pt@PdPt polyhedrons have shown an improved mass activities and area specific activities of ~ 2 A/mg_{Pt} and 3 mA/cm²_{Pt} respectively with decreased onset potential of +55 mV against 200 mV for commercial RuPt/C. Excellent and higher current stabilities of 680 mA/mg_{Pt} and 570 mA/mg_{Pt} have been obtained for two different compositions of Pt@PdPt at 0.5 V, even after 1 hour. Tolerance factor more than unity expresses their better response towards catalyst poisoning, whereas an unusual trend in this tolerance factor against cycle number (during stability tests) has been observed. We believe that employing such unique polyhedral structures of Pt skin@PdPt for the methanol electrooxidation might be a promising approach to reduce the activity loss in DMFCs.

Experimental

Hexachloroplatinic acid (H₂PtCl₆.6H₂O), palladium (II) chloride (PdCl₂), polyvinyl(2-pyrrolidone) (PVP, MW 55000), were purchased from Aldrich chemicals. Perchloric acid (HClO₄) and solvents like N-methyl 2-pyrrolidone (NMP), methanol, ethanol, ethylene glycol and acetone were purchased from Rankem chemicals. Commercial RuPt/C catalysts (comprising Pt = 32.5 wt% and Ru = 16.9

wt% with a total of 49.4 wt% loading of metal on carbon support) were purchased from Tanaka Kikinzoku Kogyo, Tokyo, Japan (TKK). Millipore water (18 M Ω) was used throughout for all methanol electrooxidation measurements.

Synthesis of Pt skin@PdPt Nanocrystals and catalyst preparation

PdPt nanocrystals have been prepared using our previous experimental procedure [51]. In brief, 5:1 mixture (volume ratio) of 25 mM PdCl₂ and 25 mM H₂PtCl₆.6H₂O solution was mixed with 15.2 mg of PVP (MW 55000, in terms of its repeating units) and dissolved properly. Then 5 mL neat NMP was added to this mixture. The mixture was stirred at 140 °C for 2 hrs. The key role in this preparation is the use of NMP (reducing solvent), which has analogous structure to that of PVP because of the amide linkages and an alkyl group attached to nitrogen. As-synthesized PdPt nanocrystals (composition of Pd₇₆Pt₂₄ determined by ICP), majority nanooctahedra, were separated and washed with water and redispersed in 5 mL NMP and used as template for further growth of Pt skin structures to prepare Pt1@PdPt. To this, a mixture containing 4.2 mmol of H₂PtCl₆.6H₂O in 1 mL of water with 2.6 mg of PVP was added. The content was stirred at 120 °C for 2 hrs followed by 1 hr at 140 °C. Complete reduction of Pt(IV) ions can be understood by monitoring the color of supernatant solution after addition of excess of acetone. This skin structure is designated as Pt1@PdPt. Similar procedure was carried out to prepare Pt2@PdPt by adding 8.4 mmol of H₂PtCl₆.6H₂O during second step growth. Pt3@PdPt nanocrystals were also prepared for comparison (but not studied in details). In order to compare the catalytic activities of such skin Pt@PdPt nanostructures and to monitor the effect of skin structure, PdPt nanocrystals with similar composition (Pd₇₂Pt₂₈ determined from ICP measurements) were prepared in a single step co-reduction process in presence of NMP and PVP maintaining the similar metal to PVP

ratio.

Finally, 25 mg of as-synthesized nanocrystals were mixed with 75 mg of carbon black (Ketjen black, EC, Surface area 800 m²/g) and were used as carbon supported Pt1@PdPt, Pt2@PdPt and PdPt catalysts. The catalysts were heat treated at 300 °C under nitrogen atmosphere to break down PVP chains into smaller amorphous analogues without serious disturbance of the shape of the nanocrystals [52]. The actual metal loading was determined by ICP-AES measurements.

Electrochemical Measurements

Glassy carbon (GC) electrode surface (geometric area: 0.0707 cm²) was polished with 0.05 μm alumina slurry, followed by careful rinsing and ultrasonication using deionized water. The electrode was coated with the active catalyst layer using a modified method from a previous report [52-53]. Briefly, 9 mg of catalyst was mixed in 12 mL of 24% IPA solution and 50 μL of nafion (5 wt %, Aldrich). Then, 4 μL aliquot of this catalyst ink was transferred to the surface of the polished and cleaned GC electrode surface. The electrode was dried under ethanol atmosphere for slow rate of evaporation. A comparative catalyst loading with literature has also been provided in Table S1 (Supporting Information). This catalyst loaded working electrode was then electrochemically cleaned by cycling between -0.25 to 1.0 V versus Ag/AgCl (sat. KCl) in N₂ saturated 0.1 M HClO₄ solution and electrochemical active surface area was determined under similar conditions prior to methanol addition on Potentiostat CHI604E. Use of H₂SO₄ as an electrolyte is avoided in present studies to rule out issues due to oxide formation or specific sulphate ion adsorption on Pt surface, though it may not affect the MOR activities to a larger extent. A Pt wire has been used as a counter electrode and all potentials mentioned throughout the discussion are referred against

Ag/AgCl. The hydrogen adsorption/desorption electric charges calculated from the CVs were used to estimate the electrochemically active surface area (ECSA) of the catalysts. It is important to note that Pd has a typical nature of absorbing hydrogen, whereas Pt adsorbs hydrogen and can be used to determine the ECSA. Hence, determination of ECSA using CO stripping technique could have been more precise methodology. Methanol electrooxidation was studied by adding appropriate amount of methanol in 0.1 M HClO₄ solution and voltammograms were recorded.

Instrumental Characterization

Inductively coupled plasma-atomic emission spectroscopy (ICP-AES) technique was used to analyze the composition, which was performed using an ICPS-8100, (Shimadzu) direct current plasma-atomic emission spectrometer. Measurements were made on emission peaks at 203.646 and 340.458 for Pt and Pd respectively. The known quantity of catalyst samples were dissolved in concentrated aqua-regia and then diluted to concentrations in the range of approx. ~100 ppm for analysis with calibration curves between 0 to 100 ppm in the same acid matrix as the unknowns. Instrument reproducibility, for concentrations greater than 100 times the detection limit, results in < 2% error. The probable compositions of present Pt1@PdPt, Pt2@PdPt and PdPt (prepared in a single step) nanocrystals using ICP-AES are found to be Pd₇₁Pt₂₉, Pd₇₀Pt₃₀ and Pd₇₂Pt₂₈ (atomic ratios have been used) along with total metal loading of 35.29 wt%, 36.25 wt% and 35.24 wt% respectively on carbon black. It is important to note that very close compositions for both the skin structures are observed. This could be due to the fact that, the addition of double the amount of chloroplatinic acid in case of Pt2@PdPt would not have changed its composition, rather atomic rearrangement at the particle-surface [Pd⁰Pt⁰ ⇌ Pt⁺⁴] might be the important phenomenon.

Transmission electron microscopic (TEM) analysis was performed on a Hitachi H-7000 electron microscope operating at 100 kV with a resolution of not less than 3-4 nm to obtain the particle size and its distribution. HRTEM study was carried out using a Topcon EM-002BF at an acceleration voltage of 200 kV. All catalysts samples before and after immobilizing on carbon support were dispersed in ethanol and drop coated on lacey carbon film-coated copper micro-grids. After drying at room temperature, these grids were then used for structural investigation.

X-ray powder diffraction (XRD) was used to measure the phase and particle sizes of the nanocrystals. XRD data were collected from $2\theta = 10-100^\circ$ with a scan rate of $2^\circ/\text{min}$ on a X'pert pro diffractometer, PANalytical using $\text{CuK}\alpha$ line ($\lambda = 1.5406 \text{ \AA}$, 40 kV, 40 mA) and the data were compared to the XRD database of PCPDF v. 2.02 (card No. 46-1043 for Pd and card No. 04-0802 for Pt) for phase identification.

Results and Discussion

Fig. 1 (a-b) illustrates low resolution TEM images of $\text{Pd}_{76}\text{Pt}_{24}$ nanocrystals along with their particle size distribution (Fig. 1c) and high resolution TEM image showing single octahedron of $\text{Pd}_{76}\text{Pt}_{24}$ (clearly shown in Fig. 1d). It can be clearly seen from low resolution image that majority of octahedra (diameter: $6.4 \pm 0.4 \text{ nm}$) are obtained with plenty of defect sites. Similarly, Fig 1(e-h) and Fig. 1 (i-l) show TEM images, particle size distribution and high resolution TEM images of for Pt1@PdPt and Pt2@PdPt respectively. Noticeable changes in the particle size and shape have been observed after second growth step, revealing a distribution of $7.5 \pm 0.5 \text{ nm}$ for Pt1@PdPt and two different distributions of $6.9 \pm 0.3 \text{ nm}$ and $7.7 \pm 0.3 \text{ nm}$ are seen in case of Pt2@PdPt . Mostly truncated cubes are grown in both the cases, indicating no effect of composition of Pt precursor on substrate particles.

Usually, bimetallic nanocrystals exhibit various geometries based on experimental conditions leading to the structures like high entropy random solid solution, low entropy cluster-in-cluster, layered, heterobond or core-shell structures [54-56]. Initial growth of PdPt alloy nanocrystals would have formed in a high entropy solid solution due to absence of any core-shell geometry during co-reduction of Pd and Pt (clearly seen in HRTEM image). A layer-by-layer type of growth mechanism is expected after a seed formation in case of PdPt alloy nanocrystals because of negligible lattice mismatch and comparable surface/interfacial energies of both the metals [18]. Simultaneous reduction of Pd and Pt ions leads to a homogeneous Pd rich alloy as seen in Scheme 1, exposing most of Pd atoms. A difference in size distribution of Pd and Pt nanocrystals is observed when reduction of separate Pd or Pt is carried out [51]. However, an intermediate size regime has been observed in case of PdPt nanocrystals, perhaps due to the contest between growth rates and seed formation. TEM images and particle size distribution of PdPt nanocrystals prepared in a single step (composition of Pd₇₂Pt₂₈) for comparison have been shown in Figure S1 in supporting information.

On the other hand, during formation of Pt skin@PdPt, the growth of the thin layer of Pt could be understood by Stransky-Krastanov mechanism, where a layer-by-layer epitaxial deposition occurs up to several monolayers. However, the dissolution of surface Pd atoms from Pd-rich PdPt nanoparticles could hamper the layer-by-layer deposition of Pt. The schematic of growth mechanism has been summarized in Scheme 1 (along with possible chemical reaction), where a systematic growth of PdPt nanoparticles is effected into truncated cubes with simultaneous dissolution of edge atoms and deposition of Pt ions at surface defect sites is shown. As a result,

surface rich Pt skin structures (Pt1@PdPt) are formed with much improved defect sites. Eventually, in presence of higher concentration of Pt, the competition between dissolution of surface Pd atoms and Pt deposition becomes much more complicated with intriguing phenomenon of Ostwald ripening, thus resulting into two different size distributions in case of Pt2@PdPt nanoparticles. A synergistic stoichiometry of Pd and Pt could have been maintained in case of Pt2@PdPt, retaining Pt rich surfaces compared to Pt1@PdPt nanoparticles. A more detailed information using high annular elemental mapping could have been obtained but we did not succeed to get such evidence owing to the thin surface Pt layer and small lattice mismatch (only 0.77%) between Pd and Pt [5]. Interestingly, all catalysts after immobilizing nanoparticles on carbon support show (Fig. 1a,e,i) excellent and homogeneous distribution of nanoparticles and should provide better electronic conduction and improved three-phase boundary for electrooxidation of methanol.

Figure 2 illustrates the comparative powder X-ray diffraction (XRD) patterns of Pt2@PdPt and Pt1@PdPt along with PdPt bimetallic nanocrystals, which are indexed to (111), (200), (220), (331) and (222) facets of a face-centred cubic lattice. The grey and green lines indicate the diffraction positions for reference Pt (PCPDF No. 04-0802 v. 2.02) and Pd (PCPDF No. 46-1043 v. 2.02) respectively for comparison, clearly exhibiting obvious changes in structural parameters for bimetallic combinations. A slight shift towards higher 2θ value in case of alloy nanocrystals indicates their lattice constant values lie between pure Pd and Pt. The lattice constant values for Pt2@PdPt, Pt1@PdPt and PdPt were found to be 3.899 Å, 3.898 Å and 3.898 Å respectively (using Vegard's law; $a_{\text{PdPt}} = x a_{\text{Pt}} + [1 - x] a_{\text{Pd}}$) assuming a composition of Pd₇₁Pt₂₉, Pd₇₀Pt₃₀ and Pd₇₂Pt₂₈ (from ICP-AES data) and

$a_{\text{Pd}} = 3.89 \text{ \AA}$ and $a_{\text{Pt}} = 3.92 \text{ \AA}$. These values also match with the values determined from XRD data at (111) plane. The crystalline domain sizes of Pt2@PdPt, Pt1@PdPt and PdPt nanocrystals are also measured as 6.0 nm, 6.2 nm and 5.5 nm respectively (using Debye-Scherrer equation). A broad peak at $2\theta=25.2^\circ$ corresponds to the carbon support.

Due to their interesting structural geometry and surface properties, these Pt skin alloy nanocrystals have been studied as anodic catalysts for methanol electrooxidation in comparison with commercial RuPt/C catalyst. Unique Pt@PdPt nanocrystals have been employed for MOR catalysis, keeping in mind enhanced MOR performance shown by Pd₁₆Pt₈₄ in our previous report [51] owing to the electronic structure modulation and formation of Pd-OH and Pt-CO retaining Pt surface free from oxygenated species directly. Figure 3(a-b) shows comparative voltammograms for both Pt skin structures Pt1@PdPt/C and Pt2@PdPt/C in presence and absence of methanol, depicting superior MOR activities of these unique structures. The blank voltammograms (without addition of MeOH) show expected features similar to polycrystalline Pt surface. Two distinct potential regions have been observed corresponding to hydrogen under potential adsorption/desorption ($\text{H}^+ + \text{e}^- = \text{H}_{\text{upd}}$) process on the nanocrystal surface. The second potential region beyond $\sim 0.5 \text{ V}$ indicates the formation of a hydroxide layer ($2\text{H}_2\text{O} = \text{OH}_{\text{ad}} + \text{H}_3\text{O}^+ + \text{e}^-$) on the catalyst surface. Electrochemical active surface area per unit weight (ECSA; m^2/g) has been determined for Pd₇₂Pt₂₈/C, Pt1@PdPt/C and Pt2@PdPt/C catalysts respectively as 48, 90 and 82 m^2/g from H_{upd} region after double layer correction and normalization to a value of 210 $\mu\text{C}/\text{cm}^2$ corresponding to the adsorbed monolayer of hydrogen on a clean polycrystalline Pt surface. A detailed

comparison of particle size, atomic ratios, metal loading and ECSA of all active catalysts and commercial RuPt/C have been provided in Table 1. Fig. 3(a and b) also clearly show the peaks corresponding to methanol oxidation at 0.54 V and similar behavior in reverse scanning at 0.45 V with curve crossing, a typical nature of methanol electrooxidation. Among, both Pt skin structures, Pt₂@PdPt structures show surprisingly higher activity compared to any other catalysts.

MOR results of Pt skin structure are also compared with that of state-of-art RuPt/C catalyst and other high surface area catalysts like Pt black. Accordingly, Figure 4(a-c) depicts the comparative MOR studies of both Pt skin structures and Pd₇₂Pt₂₈ (prepared in single step) along with commercial RuPt/C catalyst and Pt black. The mass normalized activity of Pt₂@PdPt/C in the positive direction sweep (1952 mA/mg_{Pt}) is ~8 times higher than that of RuPt/C (247 mA/mg_{Pt}), ~5 times higher than Pd₇₂Pt₂₈/C (380 mA/mg_{Pt}) and ~650 times higher than Pt black (3 mA/mg_{Pt}). A similar trend has also been observed in case of their area specific activities. Figure 4 (a) also shows a five-fold enhancement in the MOR activity of Pt skin structures compared to Pd₇₂Pt₂₈/C, revealing the prominent effect of structural changes on catalytic activity. MOR activities normalized with total active metal (Pd+Pt) loading have also been shown in Table S2 (supporting information), since all catalysts have been prepared with similar loading. This interesting trend of structural changes and MOR would support the predicted growth mechanism of optimized Pd-Pt composition at surface with Pt rich skin structures.

Furthermore, as seen in Figure 4(a-b), a tolerance factor (ratio of forward peak and backward peak potentials in MOR) of more than unity (~1.3) in both the skin structures could be attributable to the unique structures of the Pt skin structures. A similar

mechanism of bifunctional methanol oxidation mechanism for the MOR suggested by Goddard *et. al.*, can be well explained for present Pt skin structures due to presence of both Pd and Pt atoms on surface [57]. Pd is responsible for breaking the water molecule to form Pd-OH, while Pt catalyses the methanol dehydrogenation to form Pt-CO, instead of forming Pt-OH due to the presence of Pd. Nevertheless there is less theoretical assertion of Pd-OH formation, few experimental evidences [47,51] along with comparative voltammograms (shown in Fig. S2) reveal apparent changes in the Pt-OH_{ads} region (~0.6 V) after bimetallic combination. In case of Pt@PdPt, Pd-OH_{ads} is formed at a lower potential than Pt-OH_{ads} clearly indicating that the Pd is more vulnerable to oxidation changes. Consequently, the reaction between Pd-OH and Pt-CO produces CO₂ and the metal surface rejuvenates for further reaction, leading to enhancement in the activity compared to Pt alone or core-shell Pt@Pd geometries. Absence of surface Pd ions in case of core-shell Pt@Pd, makes this reaction less tolerant towards poisoning effects and therefore core Pd atoms remain under-utilized. Whereas, in present scenario, MOR is driven both thermodynamically and kinetically due to availability of desirable surface composition of Pd and Pt. For example, Figure 4(a-b) shows an onset potential of +55 mV and +120 mV for Pt₂@PdPt and Pt₁@PdPt respectively against 200 mV for RuPt, indicating a negative shift and thermodynamically favorable situation; Pt black shows onset of 125 mV against Ag/AgCl (clearly seen in Fig. S3). Water dissociation is much slower in presence of Pt alone hence shifting the potential towards more positive direction and affects the overall process adversely. On the other hand, higher Pd content also makes overall reaction more sluggish due to suppression in methanol dehydrogenation owing to lower Pt content, which can clearly be seen in case of Pd₇₂Pt₂₈/C catalyst (shown in Fig. 4a).

However, promising tolerance factor (2.33) can be observed in case of Pd₇₂Pt₂₈/C, where surface is unlikely to get easily poisoned due to less Pt content. More interestingly, although an appreciable negative shift in onset potential with increase of Pd content in PdPt alloy has been observed, current densities are decreased dramatically [51]. However, in present case, a smaller content of surface Pd has shown a tremendous effect on both onset potential as and current densities.

A comparative gain factor of MOR activity of three different Pt skin structures catalysts are given along with RuPt/C and Pd₇₂Pt₂₈/C (shown in Fig. 4c), where Pt3@PdPt (details are not given) shows again a decrease in MOR activity due to collapsing the Pt skin structures with optimum Pd:Pt ratio. Absence of Pd at surface could have been the reason for the decrease in the activity. The results have been shown in terms of both area specific (I_s) and mass specific activities (I_m) to understand the catalytic surfaces, which show a gain factor of ~8 for Pt2@PdPt against RuPt/C. A report of spatially controlled Pt-on-Pd dendrites [43] reveals an interesting structure where, both Pd and Pt can be exposed and utilized for catalytic conversion. However, the activity and onset potential values are found to be very much inferior to present Pt2@PdPt structures. Another recent study by Sun *et. al.*, [47] shows a very marginal improvement in the catalytic activity of PdPt compared to Pt/C (0.7 and 0.5 mA/cm² respectively) perhaps due to the various important parameters including, difference in preparation methods, extent of alloy formation, particle size distribution on support, the oxidation state of metals and the metal-support interactions [58]. Therefore, the synergistic effects between Pt and Pd in the alloys and surface composition with intraparticle active interfacial sites rather than particle size are very important contributing factors to determine their catalytic activities.

Current stabilities of Pt₂@PdPt and Pt₁@PdPt have been tested along with Pd₇₂Pt₂₈/C and commercial RuPt/C using single step chronoamperometry at 0.5 V against Ag/AgCl. All these catalysts have shown excellent current stability over 3600 s. As it is evident from the Figure 4(d), Pt₂@PdPt and Pt₁@PdPt show higher current stability maintaining 700 mA/mg and 560 mA/mg respectively even after 1 hour. These results indicate an initial higher current density along with less current decay at a constant potential for Pt@PdPt/C catalysts. Chronoamperometric curves also show superior current density for Pt@PdPt/C catalysts than that of RuPt/C and Pd₇₂Pt₂₈/C over entire time range. Despite well protected active sites and ideal nature due to spatially separated Pt branches (water breaking and methanol oxidation) of Pt-on-Pd dendrite structures, its stability compared to present Pt@PdPt/C is limited, which could have been due to the less alloying phenomenon and heterogeneity at hetero-interface in case of dendrite structures [21,40,43,47].

Additionally, in order to monitor the effect of Pt skin structure on mechanistically difficult C-C cleavage of C₂ type of alcohols (like ethanol and ethylene glycol), Pt₂@PdPt catalyst has also been tested for ethanol electrooxidation reaction (EOR) and ethylene glycol electrooxidation reaction (EGOR) and results are compared with MOR. Accordingly, Figure 5 indicates comparative MOR, EOR and EGOR using Pt₂@PdPt/C, showing typical nature of electrooxidation. EOR produces side products of acetaldehyde and acetic acid rather than CO_{ads}, which would eventually lead to decrease in energy utilization from ethanol, hence complete conversion of ethanol into CO₂ remains the challenge [59]. On the other hand, ethylene glycol produces side products of glycolaldehyde, glycolic acid, glyoxal, glyoxylic acid oxalic acid and suffers complete conversion to CO₂ as well [60]. Pt₂@PdPt/C shows interesting electrooxidation

behavior for all alcohols with the activity trend shown in upper inset of histogram. Among all electrooxidation reactions using Pt@PdPt/C, MOR reveals facile process, while, a better tolerance factor is observed in case of ethylene glycol electrooxidation. Lower inset of Figure 5 provides an insight of onset potentials for MOR, EOR and EGOR, where MOR has lower onset potential (+55 mV) than EOR and EGOR (+300 mV and +320 mV respectively). A significant variation in the onset potential also reveals the difficulty in breaking C-C bonds in ethanol and ethylene glycol compared to direct CO_{ads} species in case of methanol. To understand this, a parallel path mechanism for methanol oxidation has already been explained on the basis of adsorbed CO and reaction intermediates (like formaldehyde and formic acid) [61]. Besides, Langmuir-Hinshelwood model for Pt catalyst suggests a reaction between CO_{ads} and surface hydroxyl groups ($-\text{OH}_{\text{ads}}$) and methanol oxidation via CO_{ads} is promoted due to activation of water at much lower potentials in presence of Pd [62]. Therefore water activation plays an important role in increasing activity by reacting with reaction intermediate CO_{ads} leaving fresh Pt surface to make it more CO tolerant. In short, much improved and competitive results have been obtained in present work compared to recent report on multicomponent heterogeneous electrocatalysts of Pt-Pd-Rh with well defined facets [63].

Finally, Pt@PdPt bimetallic structures were tested for their stability behavior. Accordingly, to evaluate the electrocatalytic stability of Pt@PdPt/C for various electrooxidation reactions, the catalysts were cycled between -0.25 and 1.0 V up to 5000 cycles in presence of 0.1 M HClO_4 and 0.1 M methanol/ethanol/ethylene glycol. Figure 6 exhibits representative stability curves for MOR using Pt@PdPt. Usually, a decrease in the current density is observed due to surface poisoning by adsorption of organic

molecules/intermediates. Similar trend is observed in present case where a continuous decrease in the current density is observed for Pt@PdPt structures during their stability tests. Although a continuous loss in MOR activity is observed in Pt@PdPt/C system (retaining only 43% of its activity), its activity remains still higher than state-of-art catalyst RuPt/C even after 5000 cycles (clearly shown in Fig. 6b). A recent report of rhombic PtCu nanoframe structures show enhancement in the MOR activity, though the activity decreases rapidly to less than 40% even at 200th cycle indicates an unstable phase of Cu [64]. However, to the best of our knowledge, the retention of more than 60% of the catalytic activity at 3000 cycle could be a great achievement shown by Pt@PdPt structures under such poisoning conditions of reactive intermediate. Interestingly, Pt₂@PdPt and Pt₁@PdPt show slightly different behavior towards tolerance properties (Fig. S4). This trend could be attributable to the variable composition at surface. Further, as shown in Figure 6(b), Pt skin@PdPt structures show interesting conversion activities and stabilities towards MOR, EOR and EGOR even compared with highly open rhombic PtCu nanoframes [64] Pt based ordered intermetallic structures [65] and homogeneous octahedra of PdPt nanoalloy [9]. More interestingly, stability tests for EOR and EGOR indicate promising results of 70% and 58% retention of activities respectively, showing less poisoning surface for such C-C breaking (Fig. S4). Of course, a more sophisticated *in-situ* spectrometric data would have been more effective in explaining the detailed phenomenon.

Conclusions

Unique structures like Pt rich skin structures over PdPt bimetallic nanocrystals show unusual enhancement in the electrooxidation of methanol with mass activity of 1950 mA/mg_{Pt} and 3.1 mA/cm²_{Pt} along with better stability, which are much higher (8-fold

increase) compared to that of commercial RuPt catalyst, perhaps due to a better synergistic composition at surface to render facile water decomposition and further due to intraparticle active interfacial sites. Onset potentials of +55 mV and +120 mV have been observed in case of Pt₂@PdPt and Pt₁@PdPt respectively against 200 mV for RuPt indicating a thermodynamically favorable situation. Current stabilities of 700 mA/mg and 560 mA/mg at 0.5 V are shown by these active catalysts even after 1 hour along the retention of more than 60% of their catalytic activity after 5000 stability cycles. Further, exciting EOR and EGOR studies with 70% and 58% retention in activities respectively after 5000 cycles also demonstrate a facile C-C breaking in ethanol and ethylene glycol. Hence, present results show the obvious progress in designing a novel catalyst to meet the critical needs of reproducible and controllable methodology for the renewable energy applications.

Acknowledgements

Authors thank Department of Science and Technology – Science and Engineering Research Board (DST –SERB; No. SB/FT/CS-120/2012), India for financial support through Young Scientist Fast track scheme. Authors also acknowledge SRM University for providing research infrastructure.

Supporting Information

Supplementary data associated with this article can be found in the online version.

References

- (1) Y. Xia, Y. Xiong, B. Lim, S. E. Skrabalak, *Angew. Chem. Int. Ed.*, 2009, **48**, 60-103.
- (2) S. Bai, C. Wang, W. Jiang, N. Du, J. Li, J. Du, R. Long, Z. Li and Y. Xiong, *Nano Res.*, 2015 Doi: 10.1007/s12274-015-0770-6.
- (3) A. Chen and P. Hotl-Hindle, *Chem. Rev.*, 2010, **110**, 3767-3804.
- (4) N. Tian, Z. Y. Zhou, S. G. Sun, Y. Ding and Z. L. Wang, *Science*, 2007, **316**, 732-735.
- (5) S. Habas, H. Lee, V. Radmilovic, G. Somorjai and P. Yang, *Nat. Mater.*, 2007, **6**, 692-697.
- (6) S. Guo, S. Dong and E. Wang, *Chem. Commun.*, 2010, **46**, 1869-1871.
- (7) H. Wang, B. A. Kakade, T. Tamaki, T. Yamaguchi, *J. Power Sources*, 2014, **260**, 338-348.
- (8) L. Zhao, Z. -B. Wang, J. -L. Li, J. -J. Zhang, X. -L. Sui and L. -M. Zhang, *J. Mater. Chem. A*, 2015, **3**, 5313-5320.
- (9) Y. -W. Lee, A. -R. Ko, S. -B. Han, H. -S. Kim and K. -W. Park, *Phys. Chem. Chem. Phys.*, 2011, **13**, 5569-5572.
- (10) S. Cheong, J. D. Watt and R. D. Tilley, *Nanoscale*, 2010, **2**, 2045-2053.
- (11) Y. M. Li and G. Somorjai, *Nano Lett.*, 2010, **10**, 2289-2295.
- (12) H. Kobayashi, M. Yamauchi, H. Kitagawa, Y. Kubota, K. Kato and M. Takata, *J. Am. Chem. Soc.*, 2008, **130**, 1828-1829.
- (13) E. Antolini, in *Electrocatalysis of Direct Methanol Fuel Cell- From Fundamental to Applications*, ed. J. Zhang and H. Liu, Wiley-VCH Verlag GmbH & Co. KGaA, Germany, 2009, ch. 6, pp. 227-251.
- (14) B. Lim, Y. Xiong and Y. Xia, *Angew. Chem. Int. Ed.*, 2007, **46**, 9279-9282.

- (15) K. Naoe, C. Petit and M. P. Pileni, *J. Phys. Chem. C*, 2007, **111**, 16249-16254.
- (16) M. M. Coulter, J. A. Dinglasan, J. B. Goh, S. Nair, D. J. Anderson and Vy. M. Dong, *Chem. Sci.*, 2010, **1**, 772-775.
- (17) T. Teranishi and M. Miyake, *Chem. Mater.* 1998, **10**, 594-600.
- (18) Z. M. Peng and H. Yang, *Nano Today*, 2009, **4**, 143-164.
- (19) C. -Y. Chiu, Y. Li, L. Ruan, X. Ye, C. B. Murray and Y. Huang, *Nat. Chem.* 2011, **3**, 393-399.
- (20) B. Lim, M. Jiang, P. H. C. Camargo, E. C. Cho, J. Tao, X. Lu, Y. Zhu and Y. Xia, *Science*, 2009, **324**, 1302-1305.
- (21) H. Ataee-Esdahani, L. Wang, Y. Nemoto and Y. Yamauchi, *Chem. Mater.* 2010, **22**, 6310-6318.
- (22) C. Roychowdhury, F. Matsumoto, V. B. Zeldovich, S. C. Warren, P. F. Mutolo, M. J. Ballesteros, U. Wiesner, H. D. Abruna and F. J. DiSalvo, *Chem. Mater.* 2006, **18**, 3365-3372.
- (23) F. Tao, M. E. Grass, Y. Zhang, D. R. Butcher, F. Aksoy, S. Aloni, V. Altoe, S. Alayoglu, J. R. Renzas, C. -K. Tsung, Z. Zhu, Z. Liu, M. Salmeron and G. A. Somorjai, *J. Am. Chem. Soc.* 2010, **132**, 8697-8703.
- (24) S. Guo, S. Dong, and E. Wang, *ACS Nano*, 2010, **4**, 547-555.
- (25) H. Zhang, Y. Yin, Y. Hu, C. Li, P. Wu, S. Wei and C. Cai, *J. Phys. Chem.C* 2010, **114**, 11861-11867.
- (26) S. Guo, S. Zhang, X. Sun and S. Sun, *J. Am. Chem. Soc.* 2011, **133**, 15354-15457.
- (27) T. Page, R. Johnson, J. Hormes, S. Noding and B. Rambabu, *J. Electroanal. Chem.*, 2000, **485**, 34-41.
- (28) H. Yang, L. Dai, D. Xu, J. Fang and S. Zou, *Electrochimica Acta*, 2010, **55**,

8000-8004.

- (29) R. Ahmadi, M. K. Amini and J. C. Bennett, *J. Catal.*, 2012, **292**, 81-89.
- (30) T. C. Deivaraj, W. Chen and J. Y. Lee, *J. Mater. Chem.*, 2003, **13**, 2555-2560.
- (31) J. Y. Lee, D. -H. Kwak, Y. -W. Lee, S. Lee and K. -W. Park, *Phys. Chem. Chem. Phys.*, 2015, **17**, 8642-8648.
- (32) C. Xu, Q. Li, Y. Liu, J. Wang and H. Geng, *Langmuir*, 2012, **28**, 1886-1892.
- (33) H. A. Gasteiger, N. Markovic, P. N. Ross Jr. and E. J. Cairns, *J. Phys. Chem.* 1993, **97**, 12020-12029.
- (34) K. -W. Park, Y. -E. Sung, S. Han, Y. Yun and T. Hyeon, *J. Phys. Chem. B*, 2004, **108**, 939-944.
- (35) B. Lim and Y. N. Xia, *Angew. Chem. Int. Ed.*, 2011, **50**, 76-85.
- (36) H. Lee, S. E. Habas, G. A. Somorjai and P. D. Yang, *J. Am. Chem. Soc.*, 2008, **130**, 5406-5407.
- (37) B. Lim, J. G. Wang, P. H. C. Camargo, C. M. Cobley, M. J. Kim and Y. N. Xia, *Angew. Chem. Int. Ed.*, 2009, **48**, 6304-6308.
- (38) A. -X. Yin, X. -Q. Min, W. Zhu, H. -S. Wu, Y. -W. Zhang and C. -H. Yan, *Chem. Commun.*, 2012, **48**, 543-545.
- (39) X. Q. Huang, H. H. Zhang, C. Y. Guo, Z. Y. Zhou and N. F. Zheng, *Angew. Chem., Int. Ed.*, 2009, **48**, 4808-4812.
- (40) A. Demortiere and C. Petit, *Langmuir*, 2007, **23**, 8575-8584.
- (41) B. Lim, J. G. Wang, P. H. C. Camargo, M. J. Jiang, M. J. Kim and Y. N. Xia, *Nano Lett.*, 2008, **8**, 2535-2540.
- (42) H. Zhang, M. Jin, H. Liu, J. Wang, M. J. Kim, D. Yang, Z. Xie, J. Liu and Y. Xia, *ACS Nano*, 2011, **5**, 8212-8222.

- (43) L. Wang, Y. Nemoto and Y. Yamauchi, *J. Am. Chem. Soc.*, 2011, **133**, 9674-9677.
- (44) R. Srivastava, P. Mani, N. Hahn and P. Strasser, *Angew. Chem., Int. Ed.*, 2007, **46**, 8988-8991.
- (45) K. Sasaki, H. Naohara, Y. Cai, Y. M. Choi, P. Liu, M. B. Vukmirovic, J. X. Wang and R. R. Adzic, *Angew. Chem. Int. Ed.*, 2010, **49**, 8602-8607.
- (46) A. Sarakar and A. Manthiram, *J. Phys. Chem. C*, 2010, **114**, 4725-4732.
- (47) Y. Liu, M. Chi, V. Mazumder, K. L. More, S. Soled, J. D. Henao and S. Sun, *Chem. Mater.*, 2011, **23**, 4199-4203.
- (48) Y. Kang, J. Snyder, M. Chi, D. Li, K. L. More, N. M. Markovic and V. R. Stamenkovic, *Nano Lett.*, 2014, **14**, 6361-6367.
- (49) Y. Wu, D. Wang, G. Zhou, R. Yu, C. Chen and Y. Li, *J. Am. Chem. Soc.*, 2014, **136**, 11594-11597.
- (50) L. Han, H. Liu, P. Cui, Z. Peng, S. Zhang and J. Yang, *Sci. Rep.*, 2014, **4**, 6414/1-6414/16.
- (51) B. A. Kakade, T. Tamaki, H. Ohashi and T. Yamaguchi, *J. Phys. Chem. C*, 2012, **116**, 7464-7470.
- (52) Y. Borodko, H. S. Lee, S. H. Joo, Y. Zhang and G. Somorjai, *J. Phys. Chem. C*, 2010, **114**, 1117-1126.
- (53) Y. Garsamy, O. A. Baturina, K.E. Swider-Lyons and S. S. Kocha, *Anal. Chem.*, 2010, **82**, 6321-6328.
- (54) T. Teranishi and N. Toshima in *Catalysis and Electrocatalysis at Nanoparticle Surfaces* ed. A. Wieckowski, E. R. Savinova, C. C. Vayenas, Marcel Dekker, New York, 2003, ch. 11, pp. 379-408.

- (55) N. Toshima, *Polymer-capped bimetallic nanoclusters as active and selective catalysts*, in *Macromolecular Nanostructured Materials* ed. N. Ueyama and A. Harada, Kodansha/Springer, Japan/Berlin, Germany, 2004, ch. 3.3, pp. 182.
- (56) C.-R. Bian, S. Suzuki, K. Asakura, P. Lu and N. Toshima, *J. Phys. Chem. B*, 2002, **106**, 8587-8598.
- (57) J. Kua and W. A. Goddard, *J. Am. Chem. Soc.*, 1999, **121**, 10928-10941.
- (58) F. Şen and G. Gökagaç, *J. Phys. Chem. C*, 2007, **111**, 5715-5720.
- (59) F. Vigier, C. Coutanceau, F. Hahn, E. Belgsir and C. Lamy, *J. Electroanal. Chem.* 2004, **563**, 81-89.
- (60) J. Schnaidt, M. Heinen, Z. Jusys and R. J. Behm, *J. Phys. Chem. C*, 2012, **116**, 2872-2883.
- (61) H. Wang, T. Löffler and H. Baltruschat, *J. Appl. Electrochem.*, 2001, **31**, 759-765.
- (62) J. -M. Léger, S. Rousseau, C. Coutanceau, F. Hahn and C. Lamy, *Electrochim. Acta*, 2005, **50**, 5118-5125.
- (63) W. Zhu, J. Ke, S. -B Wang, J. Ren, H. -H. Wang, Z. -Y. Zhou, R. Si, Y. -W. Zhang and C. -H. Yan, *ACS Catal.* 2015, **5**, 1995-2008.
- (64) J. Ding, X. Zhu, L. Bu, J. Yao, J. Guo, S. Guo and X. Huang, *Chem. Commun.*, 2015, **51**, 9722-9725.
- (65) E. C. -Rivera, D. J. Volpe, L. Alden, C. Lind, C. Downie, T. V. -Alvarez, A. C. D. Angelo, F. J. DiSalvo and H. D. Abruña, *J. Am. Chem. Soc.* 2004, **126**, 4043-4049.

Figure Captions

Scheme 1. Schematic of the two-step growth of Pt thin layer on PdPt in presence of NMP and PVP along with possible chemical reaction.

Table 1. Comparison of particle size, atomic ratios, metal loading and ECSA of Pt skin bimetallic nanocrystals with PdPt and commercial RuPt nanocrystals.

Figure 1. Low resolution TEM images of (a & b) Pd₇₆Pt₂₄/C and Pd₇₆Pt₂₄ nanocrystals with (c) size distribution histogram (diameter: 6.4±0.4 nm) and (d) high resolution image and schematic (Pd: yellow and Pt: red balls) of single Pd₇₆Pt₂₄ octahedron; low resolution TEM images of (e & f) Pt1@PdPt/C and Pt1@PdPt nanocrystals with (g) size distribution histogram (diameter: 7.5±0.5 nm) and (h) high resolution image and schematic of single Pt1@PdPt cuboctahedron; low resolution TEM images of (i & j) Pt2@PdPt/C and Pt2@PdPt nanocrystals with (k) size distribution histogram (diameter: 6.9±0.3 nm & 7.7±0.3 nm) and (l) high resolution image and schematic of single Pt2@PdPt cuboctahedron; *d* - spacing in all cases is found to be 0.225 nm corresponds to {111} planes.

Figure 2. XRD patterns of Pt2@PdPt, Pt1@PdPt and PdPt bimetallic nanocrystals revealing fcc packing of the atoms with obvious changes in diffraction patterns, in comparison to reference diffraction positions of Pt (grey lines) and Pd (green lines); inset showing clear differences in (111) planes of all catalysts.

Figure 3. (a & b) Superimposed cyclic voltammetric curves for Pt2@PdPt and Pt1@PdPt respectively in 0.1 M HClO₄ in presence and absence of 0.1 M MeOH under saturated nitrogen conditions.

Figure 4. (a) Comparative mass activities of Pt2@PdPt and Pt1@PdPt and Pd₇₂Pt₂₈ towards methanol electro-oxidation (b) comparative mass activities of Pt2@PdPt and

Pt1@PdPt and commercial RuPt and Pt black towards methanol electro-oxidation; (c) activity gain factor for various catalysts towards methanol electro-oxidation (I_s = area specific activity and I_m = mass specific activity); (d) current stability at 0.5 V by chronoamperometry in 0.1 M HClO₄ and 0.1 M MeOH under N₂ atmosphere.

Figure 5. Comparative electrooxidation of methanol (MOR), ethanol (EOR) and ethylene glycol (EGOR) at Pt2@PdPt/C surface, showing typical behavior of electrooxidation of all alcohols; upper inset revealing better performance of Pt2@PdPt towards MOR than EOR and EGOR; lower inset indicates variation in the onset values.

Figure 6. (a) Representative stability test for Pt2@PdPt towards MOR with potential cycling up to 5k (b) stability of P2@PdPt towards MOR, EOR and EGOR, revealing better MOR performance by Pt2@PdPt structures.

Scheme 1.

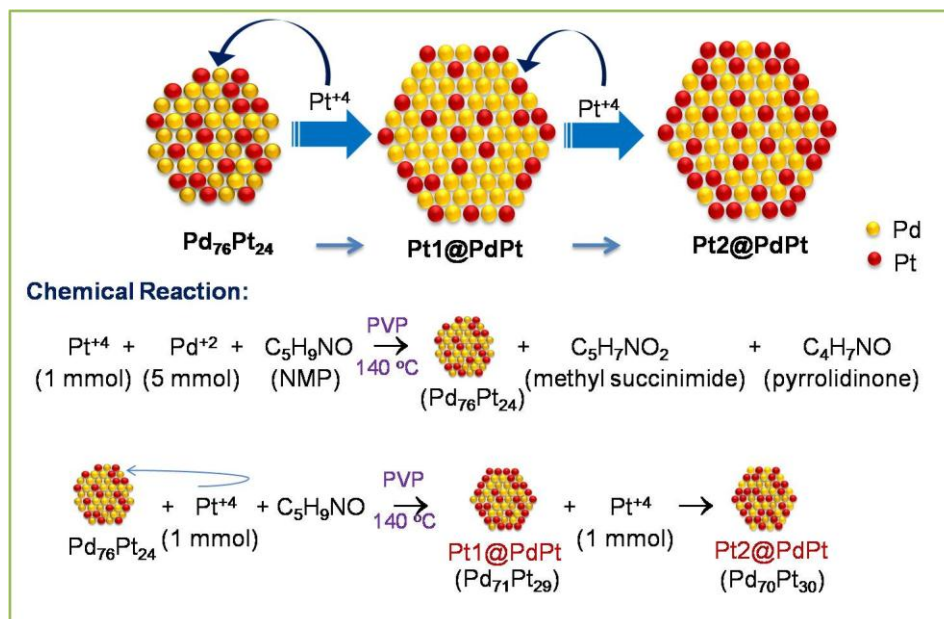


Table 1.

Catalyst	Particle Size (nm)	Empirical formula (Atomic ratio)	Metal loading (Pt+Pd) on carbon black (wt%)	Pt loading on GC ($\mu\text{g}/\text{cm}^2$)	Total metal loading on GC ($\mu\text{g}/\text{cm}^2$)	ECSA ($\text{m}^2/\text{g}_{\text{Pt}}$)
Pt1@PdPt	7.5 \pm 0.5	Pd ₇₁ Pt ₂₉	35.29	6.91	16.31	90
Pt2@PdPt	6.9 \pm 0.3; 7.7 \pm 0.3	Pd ₇₀ Pt ₃₀	36.25	7.48	17.11	82
PdPt	6.6 \pm 0.5	Pd ₇₂ Pt ₂₈	35.24	6.22	15.77	48
RuPt Comm	1.00 to 5.00	Ru ₇₉ Pt ₂₁	Pt+Ru = 49.4	14.26	21.68	52

Figure 1.

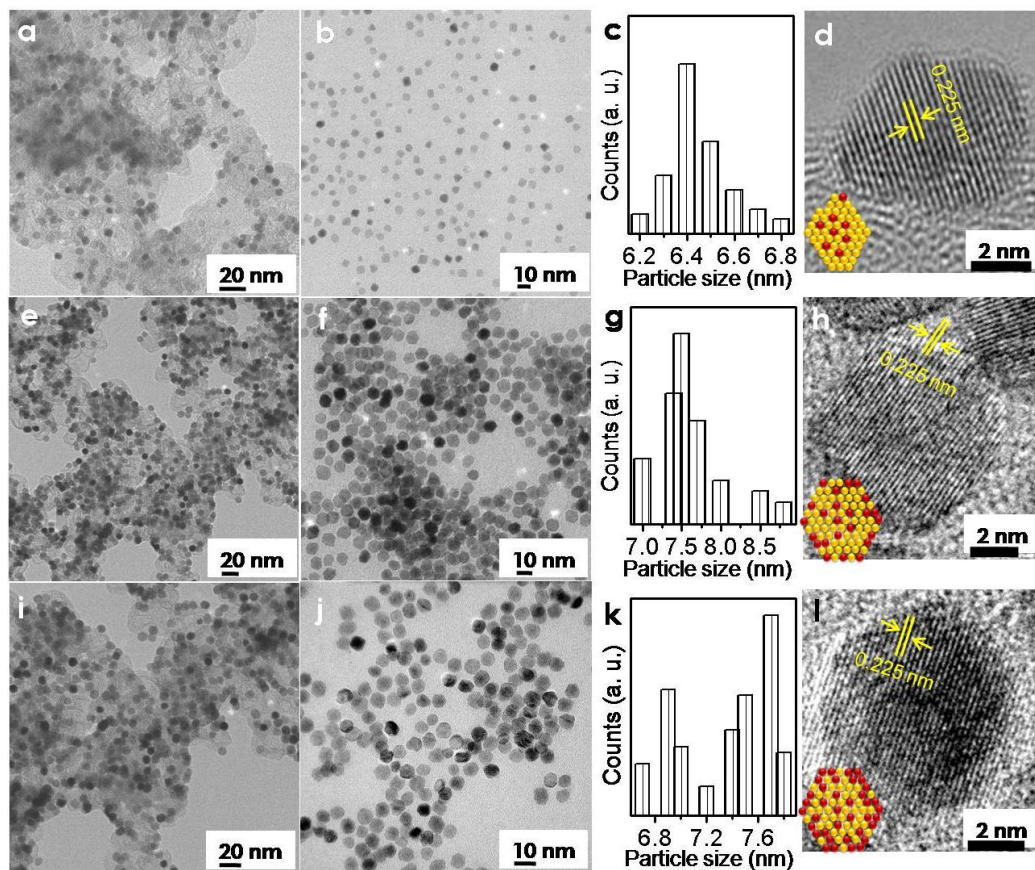


Figure 2.

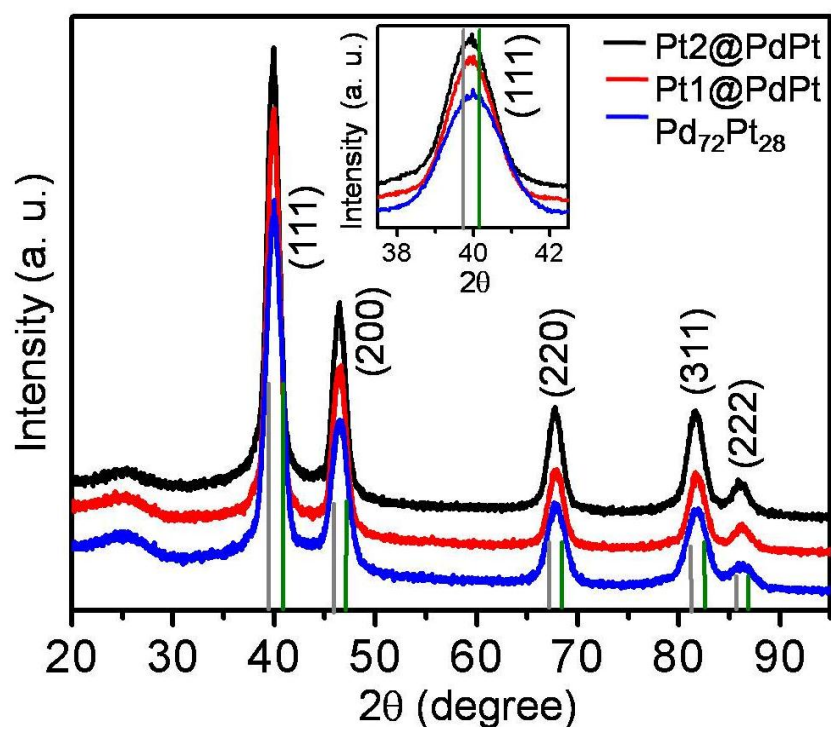


Figure 3.

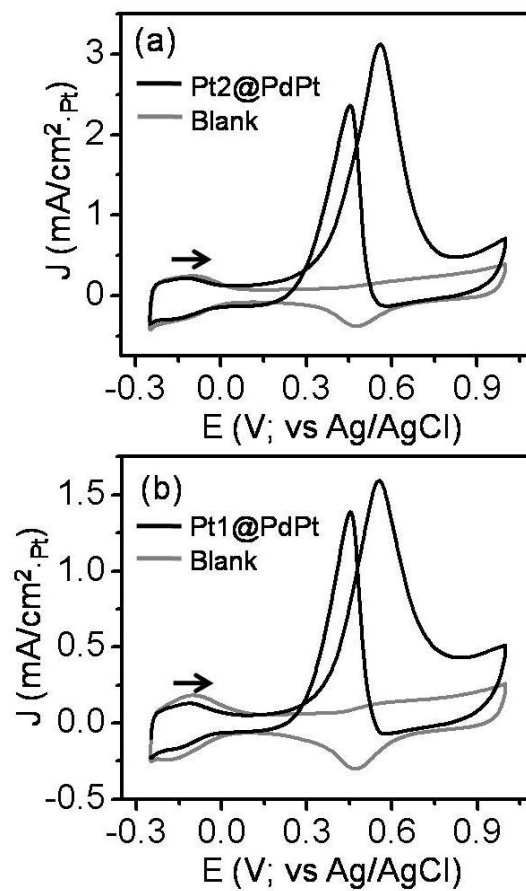


Figure 4.

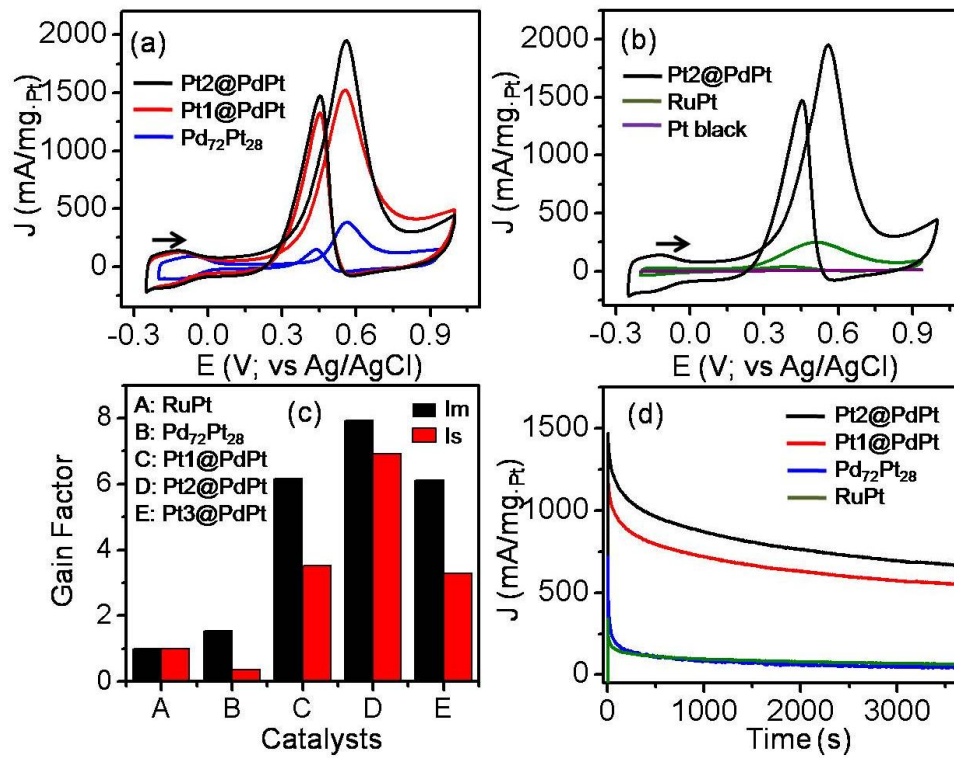


Figure 5.

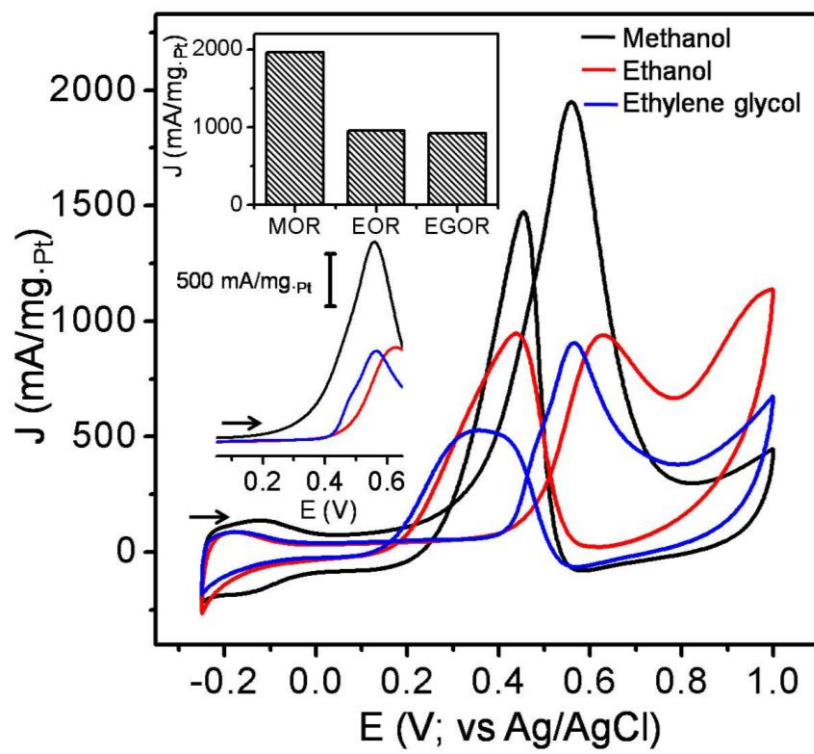
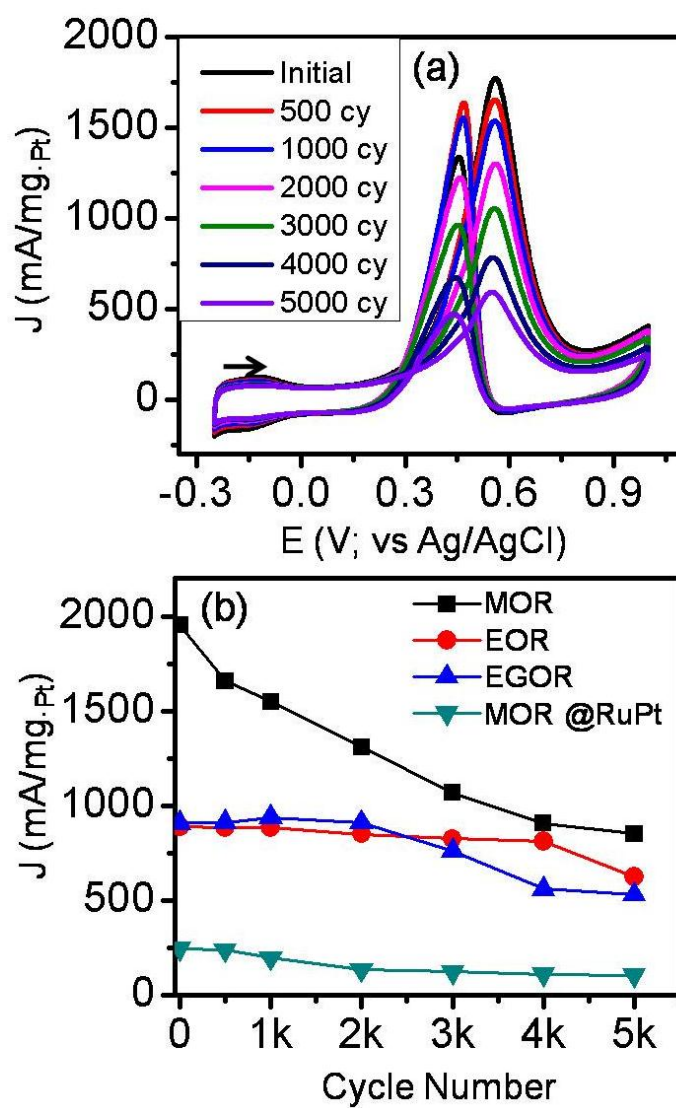
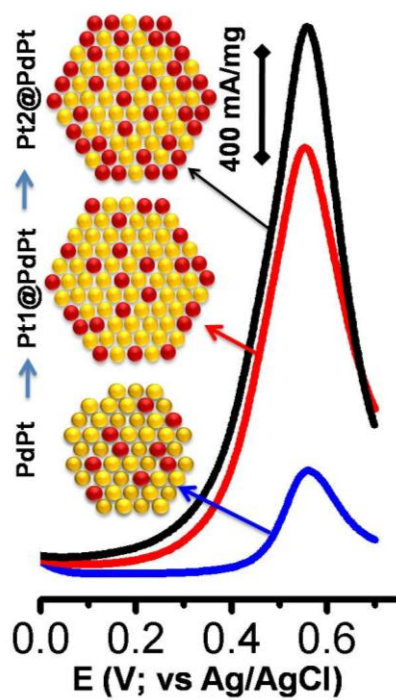


Figure 6.



TOC Graphical Abstract



Pt skin structures over PdPt bimetallic nanocrystals show unusual enhancement in the methanol electrooxidation with mass activity of 2000 mA/mg_{Pt} and better stability.